




Cite this: *Mater. Adv.*, 2023,  
4, 2466

Received 1st April 2023,  
Accepted 29th April 2023

DOI: 10.1039/d3ma00150d

rsc.li/materials-advances

## Enhancing sound insulation of glass interlayer films by introducing piezoelectric fibers†

Donghe Chen, Shuo Zheng, Mingyu Jing, Zaiqian Yu, Jiawei Zhang, Longjiao Yu, Shulin Sun  and Shiwei Wang \*

Traditional polyvinyl butyral (PVB)-laminated glass could not satisfy the rising requirements of sound insulation due to the mass law, especially in the low-frequency region. In this study, a new strategy that uses piezoelectric fibers to improve the sound insulation of materials is first proposed. Polyvinylidene fluoride (PVDF)/multi-walled carbon nanotube (MWCNT) membranes were prepared by electrospinning. Thereafter, laminated glass with glass/PVB/PVDF/PVB/glass structure was successfully constructed by the hot pressing process. 30 pC/N of the maximum piezoelectric coefficient ( $d_{33}$ ) and 2 V of the maximum output voltage for the PVDF/MWCNT membrane were achieved. The PVB/PVDF composite glass interlayer film could break the conventional mass law with a transmission loss of over 15 dB in the low-frequency region (200–500 Hz). On average, 48% passing through sound energy was reduced than that for the pure PVB film, which indicated the effective block out of human noise. The excellent transmittance and impact resistance of the composite laminated glass were also confirmed from the ultraviolet spectrum and falling ball impact test, respectively. It is of great significance to the research and development of sound insulation materials.

## Introduction

In recent years, increasing attention has been attracted to noise pollution, which may cause hearing loss, sleep disorders, and other symptoms.<sup>1–3</sup> Several methods have been adopted to eliminate noise, among which, sound insulation materials with damping and shock-absorbing functions take the dominant part.<sup>4</sup> As an excellent damping material, polyvinyl butyral (PVB) has been widely used in laminated glass depending on its strong adhesion, high transparency, and impact resistance.<sup>5–8</sup> The long molecular chain of PVB is prone to curl and entangle under the excitation of sound energy. The chain segments in the molecule move and slip and generate internal friction, which can convert sound energy into heat, thus eliminating noise and achieving sound insulation.<sup>9</sup>

PVB laminated glass is constructed by sandwiching PVB film between two or more glass substrates by a hot pressing process.<sup>10</sup> The common deficiency of traditional sound insulation materials, is the unsatisfactory sound insulation in the low-frequency region, especially for blocking human noise. Yet it is not a good solution to increase the thickness of glass

because of weight limits. Therefore, it is a challenge to develop a light and simple sound-insulating laminated safety glass. Recently, a new strategy for converting sound energy into electric energy has been proposed.<sup>11,12</sup> Sound energy is first transferred to the piezoelectric material and converted into electric potential energy through the piezoelectric effect. Then electric energy is further converted into heat energy through the conductive network. Piezoelectric polymer materials, such as polyvinylidene fluoride (PVDF), have been widely investigated owing to their high piezoelectric coefficient, lightweight, and strong mechanical properties that facilitate their application in complex structures.<sup>13–15</sup>

PVDF has five crystalline forms with three conformations: (1) all-trans (TTTT) planar zigzag for the  $\beta$  phase, (2) TG + TG- for the  $\alpha$  and  $\delta$  phases, and (3) T3G + T3G- for  $\gamma$  and  $\epsilon$  phase.<sup>16–18</sup> The  $\beta$  phase has the highest polarization per unit cell, which is decisive for the piezoelectricity of PVDF polymers.<sup>19</sup> The nonpolar  $\alpha$  phase that is formed spontaneously could be converted into  $\beta$  phase through various post-treatments, such as high electric field poling, mechanical stretching, and quenching at higher rates.<sup>20</sup> Blending PVDF with conductive additives is also a common method to improve piezoelectricity.<sup>21</sup> Multi-walled carbon nanotubes (MWCNTs) have been widely used owing to their high aspect ratios and electron-rich large surface areas.<sup>22–24</sup> It is well-recognized that well-dispersed MWCNTs can significantly improve the piezoelectricity of PVDF.<sup>25,26</sup> The piezoelectric PVDF/MWCNT

School of Chemical Engineering, Advanced Institute of Materials Science,  
Changchun University of Technology, Changchun 130012, P. R. China.  
E-mail: wswjldx2004@163.com

† Electronic supplementary information (ESI) available. See DOI: <https://doi.org/10.1039/d3ma00150d>



composites have the potential to be applied in many fields owing to the excellent electrical properties of MWCNTs and the efficient  $\alpha$  to  $\beta$  phase transformation during the electrospinning (ES) process.<sup>27</sup> The ES/PVDF membrane has excellent piezoelectricity through electric field poling and stretching while retaining high porosity and specific surface area. Wu and Chou demonstrated that ES piezoelectric PVDF/CNT membrane is an efficient sound absorption material.<sup>28</sup> However, the relationship between the piezoelectricity of fibers and sound insulation has not been reported. It is an effective solution to improve the low-frequency sound insulation of laminated glass by incorporating electrospun piezoelectric fibers with negligible mass into the damping material of PVB.

In this work, PVDF composite membranes were produced by ES technology. The piezoelectric coefficient and output voltage of the PVDF membranes were greatly improved by the introduced MWCNTs. Then, the composite membrane was incorporated into PVB films by the hot pressing process. The transmission loss of the PVB/PVDF composite film is significantly enhanced in the low-frequency region and the enhancement can be reached a maximum of 3.6 dB compared to that of pure PVB film. The average passing through sound energy is significantly reduced, which means that human noise can be effectively blocked out. The results show that the sound insulation performance of the composite films is related to the piezoelectricity of fibers and demonstrate the feasibility of employing piezoelectric fibers for sound insulation. Then, laminated glass based on PVB/PVDF composite film was also constructed by hot pressing. Its transmittance reaches nearly 80%, which is attributed to efficient energy conversion. The excellent impact resistance of the composite laminated glass was also confirmed by a breakage rate of less than 3.0%. This lightweight and solid laminated glass with good sound insulation can be widely used in many fields.

## Experimental methods

### Materials

PVDF powders (Kynar<sup>®</sup> 761) with a molecular weight of 500 000 were supplied by Arkema China Co., Ltd. *N,N*-dimethylformamide (DMF, AR) and acetone (AC, AR) were purchased from Sigma Aldrich Co., Ltd. MWCNTs with an inner diameter of 5–10 nm, an outer diameter of 20–30 nm, and a length of 10–30  $\mu$ m were purchased from Aladdin Reagent Co., Ltd, and PVB films were produced by tape casting extrusion process in our research group. All materials and solvents were used directly without any purification.

### Sample preparation

MWCNTs were dispersed in the solvent mixture of 3 mL DMF and 2 mL AC, and sonicated for 1 hour. Then, a solution containing 18 wt% of PVDF/MWCNTs was obtained by adding PVDF powders to MWCNTs solution at 50 °C with stirring for 30 min.

PVDF/MWCNTs membranes with 10  $\mu$ m of thickness were produced by ES at a voltage of 15 kV, 1 mL h<sup>-1</sup> of flowing rate, and 20 cm distance between needle tip (1.36 mm diameter) and

collector. The PVB/PVDF composite based on PVB/PVDF/PVB structure was constructed by sandwiching the PVDF membrane between two PVB films (0.38 mm) with 3 mm glass on the outer side by hot pressing at 130  $\pm$  1 °C and 1.5  $\pm$  0.1 Mpa.

### Characterization

The morphology of electrospun PVDF/MWCNTs membranes was observed using a scanning electron microscope (SEM, JSM-7610F, Japan) at 5 kV and transmission electron microscope (TEM, TECNAI, F20, USA) at 200 kV. The dispersion of MWCNTs was observed using an optical microscope (Phoenix, XSP-36-1600X, China). The conductivity of the composite membrane was measured using an electrochemical workstation (PGSTAT302N, Auto lab). The dielectric test system (CPE1901, Polyk) was used to measure the dielectric constant of the composite membrane. Fourier transform infrared spectroscopy (FT-IR, Thermofisher Nicolet, USA) scans were recorded over a range of 1500–650 cm<sup>-1</sup>. During differential scanning calorimetry (DSC, Mettler Toledo, America), the electrospun PVDF nanofiber membrane was scanned from 25 to 250 °C at a rate of 10 °C min<sup>-1</sup> and then maintained under isothermal conditions for 5 min at 250 °C. Optical transmittance spectra were obtained on a UV-vis spectrophotometer (Agilent Cary 5000, USA) within the range of 200–1000 nm. The impact resistance of the laminated glass was tested using the falling ball impact tester (SHALA-KCJ-28).

Type SW-422 Impedance tubes (BSWA Technology Co., Ltd) were used to characterize the transmission loss of the composite film in the range of 64–1600 Hz according to the transfer matrix method specified in ASTM E2611-19. The power amplifier was connected to the impedance tube to provide sound. Four fixed-position microphones measured the sound pressure level and transmitted the data to the data acquisition system, and the transmission loss was calculated by the noise and vibration testing system (Va-Lab). The composite film was cut to the required size (114 mm in diameter) by using an electric punching machine.

## Results and discussion

The morphology of the electrospun PVDF membranes with and without the MWCNTs are shown in Fig. 1a–e. It can be seen from Fig. 1f that the average diameter of the fibers was reduced from 800  $\pm$  200 nm to 400  $\pm$  150 nm when 0.1 wt% MWCNTs were added. The decrease may be attributed to the excellent electrical properties of the MWCNTs that resulted in the higher charge density of the solution in the nozzle and larger splaying of the electrified jet.<sup>29</sup> However, the average diameter increased to 830  $\pm$  200 nm with the increase in the loading of MWCNTs due to the increased viscosity of the electrospun solution. As shown in Fig. S1 (ESI<sup>†</sup>), the MWCNTs were well dispersed in the PVDF membrane when the loading was less than 0.5 wt% (Fig. S1a–c, ESI<sup>†</sup>). However, a large amount of agglomeration of MWCNTs can be seen when the loading increased to 1.0 wt% (Fig. S1d, ESI<sup>†</sup>). It shows that ultrasound was not enough to break the bond between each CNT, and the high viscosity of the



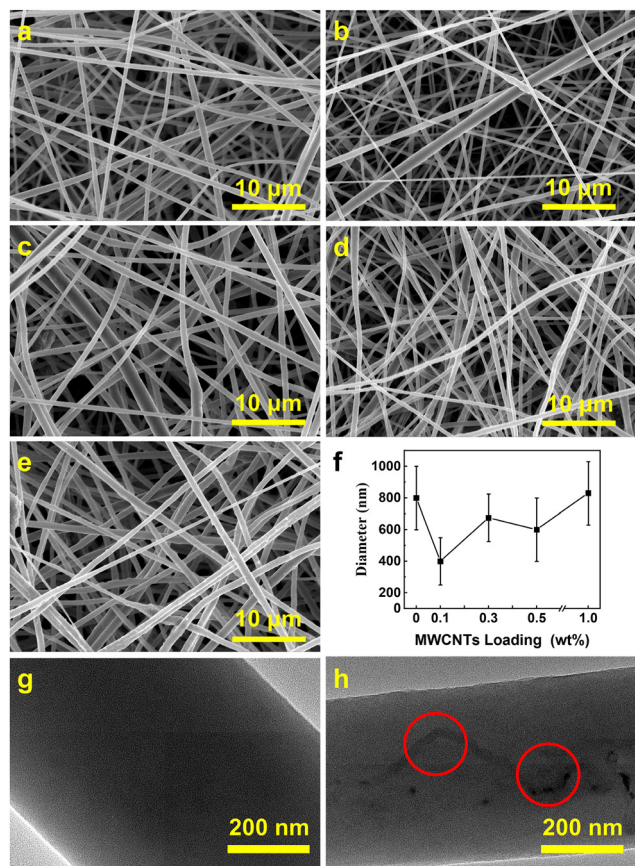


Fig. 1 SEM images of the electrospun PVDF membranes with (a) 0% (b) 0.1 wt%, (c) 0.3 wt%, (d) 0.5 wt%, and (e) 1.0 wt% MWCNTs. (f) The average diameters of PVDF/MWCNTs nanofibers with different MWCNTs loads. TEM images of electrospun (g) PVDF and (h) PVDF/MWCNTs membranes.

solution was difficult to offset due to the limited voltage driving force.<sup>30</sup> It can be seen from the TEM images shown in Fig. 1g and h that more MWCNTs were embedded within each PVDF nanofiber rather than dispersed outside. Electrospun PVDF/MWCNTs membranes were thus successfully produced. The specific surface area and porosity of all the electrospun fiber membranes were measured using a Tristar II 3020, Micromeritics, instrument. It can be seen from Table S1 (ESI<sup>†</sup>) that the Brunauer-Emmett-Teller (BET) surface area of the sample decreased from 4.3447 to 0.0110 m<sup>2</sup> g<sup>-1</sup> with the increase in a load of MWCNTs, which is attributed to the increase of fiber diameter. The pore volume decreased significantly, especially, when the loading of MWCNTs reached 0.3 wt%. The pore size also increased from 4.3528 to 119.6159 Å when 1.0 wt% MWCNTs were added. This seems to be detrimental to low-frequency sound insulation because high specific surface area and porosity meant a high probability of sound waves colliding with fibers, thereby absorbing sound energy. The relevant data will be discussed later.

The electrical properties of electrospun PVDF/MWCNTs Membranes were characterized, and the data is shown in Fig. 2a. It shows that the conductivity of the composite membrane increases slightly when the loading of MWCNTs was below 0.3 wt%, which is attributed to the excellent conductivity of

MWCNTs. As the loading of MWCNTs was increased to 0.5 wt%, an abrupt increase (about 10<sup>-8</sup> to 10<sup>-3</sup>) in conductivity appeared, which is attributed to a typical percolation threshold.<sup>31</sup> That means the conductive network was completely formed in the PVDF membrane. However, the decrease in conductivity can be observed when 1.0 wt% MWCNTs were added. This is consistent with the previous conclusion (Fig. 1) that excess MWCNTs will agglomerate and hinder the formation of a conductive network.

The dielectric constant of composite membranes in the frequency range of 10<sup>2</sup> to 10<sup>6</sup> Hz at room temperature are shown in Fig. 2b. At low frequencies, much higher dielectric constant can be obtained for the composite membranes. In addition, the dielectric constant of all composite membranes will decrease with the increase of the frequency. The law of dielectric constant is consistent with that of conductivity. The maximum dielectric constant for the composite membranes is about 120 when the loading of MWCNTs increases to 0.5 wt%, which is much higher than that of pure PVDF membrane with 11. To sum up, the addition of MWCNTs increases the conductivity of the composite membranes, and its uniform dispersion contributes to reinforcement of the dielectric property, which means higher polarization efficiency in the electric field.<sup>32</sup>

Fig. S2 (ESI<sup>†</sup>), shows the diffraction angle of electrospun pure PVDF and PVDF/MWCNTs membrane with different MWCNTs loads at 20 kV were characterized by X-ray diffraction (XRD) from a scan range of 5° to 50°. The samples showed an intense peak around 20.6° ((110) reflection)<sup>33</sup> corresponding to β and a small hump at 18° indicating the existence of α phase in the electrospun fiber membrane. The XRD results are further supported by FTIR, as shown in Fig. 2c, intercepted from Fig. S3 (ESI<sup>†</sup>), and the crystalline phase of PVDF was quantitatively calculated. The bands observed at 976, 764, and 613 cm<sup>-1</sup> can be attributed to the α phase of PVDF, whereas the bands at 840 and 1275 cm<sup>-1</sup> can be attributed to the β phase.<sup>34</sup> The relative β phase fraction of PVDF samples *F*(β) was calculated using eqn (1) derived from the Beer-Lambert law:

$$F(\beta) = \frac{X_{\beta}}{X_{\alpha} + X_{\beta}} = \frac{A_{\beta}}{\left(\frac{K_{\beta}}{K_{\alpha}}\right)A_{\alpha} + A_{\beta}} = \frac{A_{\beta}}{1.3A_{\alpha} + A_{\beta}} \quad (1)$$

where *A*<sub>α</sub> and *A*<sub>β</sub> are the absorption values at 764 cm<sup>-1</sup> and 840 cm<sup>-1</sup>, respectively, *K* is the absorption coefficient at each wave number, and the values of *K*<sub>α</sub> and *K*<sub>β</sub> are 6.1 × 10<sup>4</sup> and 7.7 × 10<sup>4</sup> cm<sup>2</sup> mol<sup>-1</sup>, respectively.<sup>35</sup> With increasing of MWCNTs loading, *F*(β) values for electrospun PVDF membranes were 78%, 70%, 67%, 69% and 63%, respectively. It can be concluded that the most common α phase can be efficiently converted into β phase by ES, but the decrease of *F*(β) was observed when the loading of MWCNTs increases. On one hand, the addition of MWCNTs promotes the charge accumulation at the interface, arranging PVDF chains in the β phase conformation. On the other hand, the entanglement of MWCNTs and PVDF molecular chains hinders the crystallization of PVDF during the solidification process, thus reducing β phase transformation.<sup>36</sup> The *d*<sub>33</sub> of electrospun PVDF/MWCNTs membranes was measured using a piezoelectric





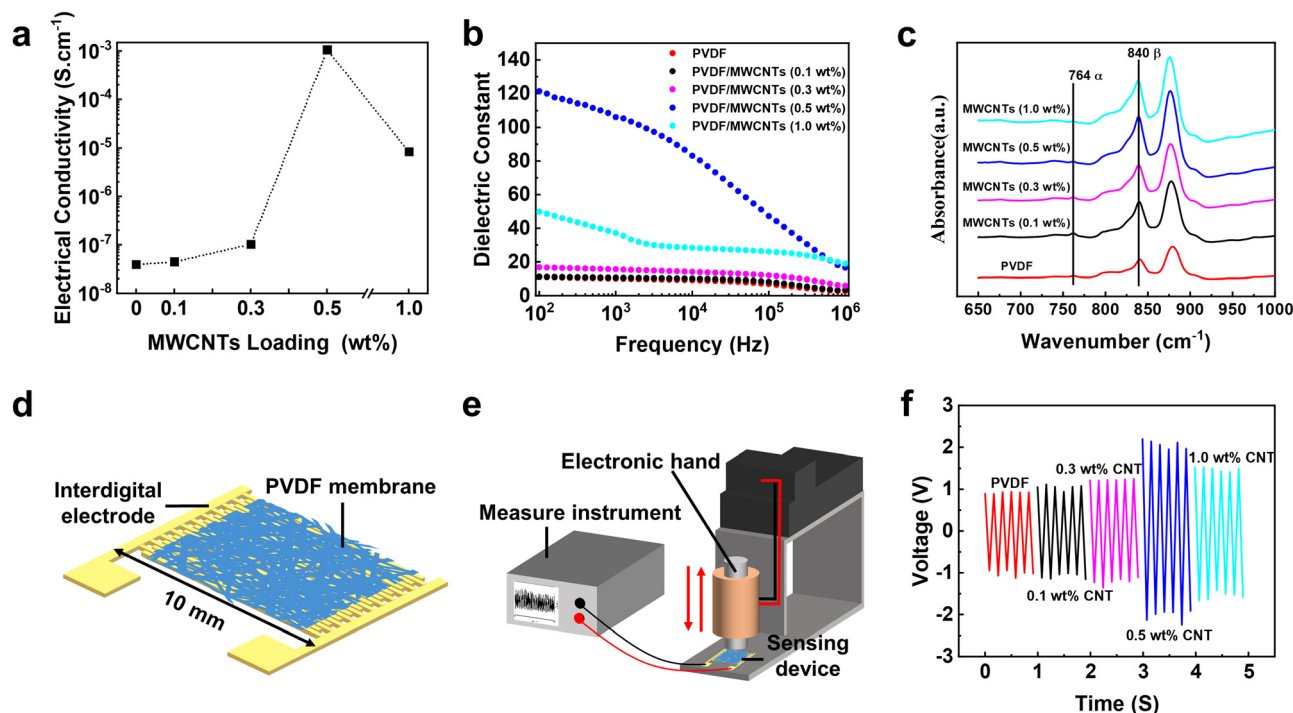


Fig. 2 (a) Electrical conductivity and (b) the dielectric constant of electrospun PVDF/MWCNTs membranes with different MWCNTs loads. (c) FT-IR spectra of electrospun PVDF and PVDF/MWCNTs membranes. (d) Sensing device and (e) an illustration of the test platform. (f) The output voltage for the electrospun PVDF/MWCNTs membranes.

coefficient meter (ZJ-3AN, China). The  $F(\beta)$  and piezoelectric coefficient  $d_{33}$  are listed in Table 1. In the PVDF/MWCNTs system, MWCNTs loading of 0.1 wt% are superior to pure PVDF membrane. The  $d_{33}$  increased by 17–30 when 0.1–0.5 wt% was added. Its  $d_{33}$  decreases when the loading of MWCNTs increases to 1.0 wt%. This is attributed to the decrease in its conductivity and dielectric constant, which led to the decrease in polarization efficiency. In addition, the mobile charges that facilitate polarization were also reduced because of the agglomeration of MWCNTs. The piezoelectricity of electrospun PVDF/MWCNTs membranes was also measured using a photovoltaic source measure instrument (Keithley 2450). As shown in Fig. 2d, a sensing device was assembled by compressing an electrospun PVDF/MWCNTs membrane on an interdigital electrode with an area of 10 mm  $\times$  10 mm. Then, an electronic hand with a frequency of 10 Hz was used for cyclic induction of the sensor. Output signals were recorded at the other end (Fig. 2e). The output electric potentials for the electrospun PVDF/MWCNTs membranes are shown in Fig. 2f and Fig. S4 (ESI<sup>†</sup>). The average output voltages and currents were detected from 0.9 to 1.5 V and

0.45 to 1.0 nA, corresponding to the electrospun composite membranes with 0 wt% to 1.0 wt% of MWCNTs loadings, respectively. The generated output peaks were at 2.0 V and 1.2 nA when MWCNTs loading was 0.5 wt%. The result further evidenced that 0.5 wt% MWCNTs is the best doping amount to improve the piezoelectricity, which is consistent with the  $d_{33}$  characterization. The results show that the introduction of MWCNTs improves the piezoelectricity of electrospun PVDF membranes.

As shown in Fig. 3a, the composite films with PVB/PVDF/PVB structure were constructed by the hot pressing process, Fig. S5 (ESI<sup>†</sup>) presents the thermogram of the electrospun PVDF nanofiber membrane, the melting point of PVDF (about 168  $^{\circ}\text{C}$ ) is higher than the hot pressing temperature (130  $^{\circ}\text{C}$ ), so the electrospun PVDF membrane will not be affected. The transmission loss (TL) of the composite films in the low-frequency region was measured using an acoustical measurement system, as shown in Fig. S6a (ESI<sup>†</sup>). Fig. S6b (ESI<sup>†</sup>) is the image of the sample. TL curves of PVB/PVDF composite films shown in Fig. 3b could be divided into three regions: stiffness control region, damping control region, and mass control region. The stiffness control region from 64 Hz to 180 Hz is generally shown as a downward-sloping curve, in which the TL of the sample is related to the sample size, stiffness, and the connection state with the instrument. The damping control region from 180 Hz to 200 Hz is related to the damping characteristics of the sample. In this region, their TL reaches the minimum value. TL in both regions cannot reflect the real sound insulation performance of the sample. The mass control region from 200 Hz to 500 Hz is an oblique upward straight line, which is

Table 1  $F(\beta)$  values and piezoelectric coefficient of the PVDF samples

Sample	$F(\beta)$ (%)	$d_{33}$ (pC/N)
PVDF	78	15
PVDF/MWCNTs (0.1 wt%)	70	17
PVDF/MWCNTs (0.3 wt%)	67	20
PVDF/MWCNTs (0.5 wt%)	69	30
PVDF/MWCNTs (1.0 wt%)	63	26

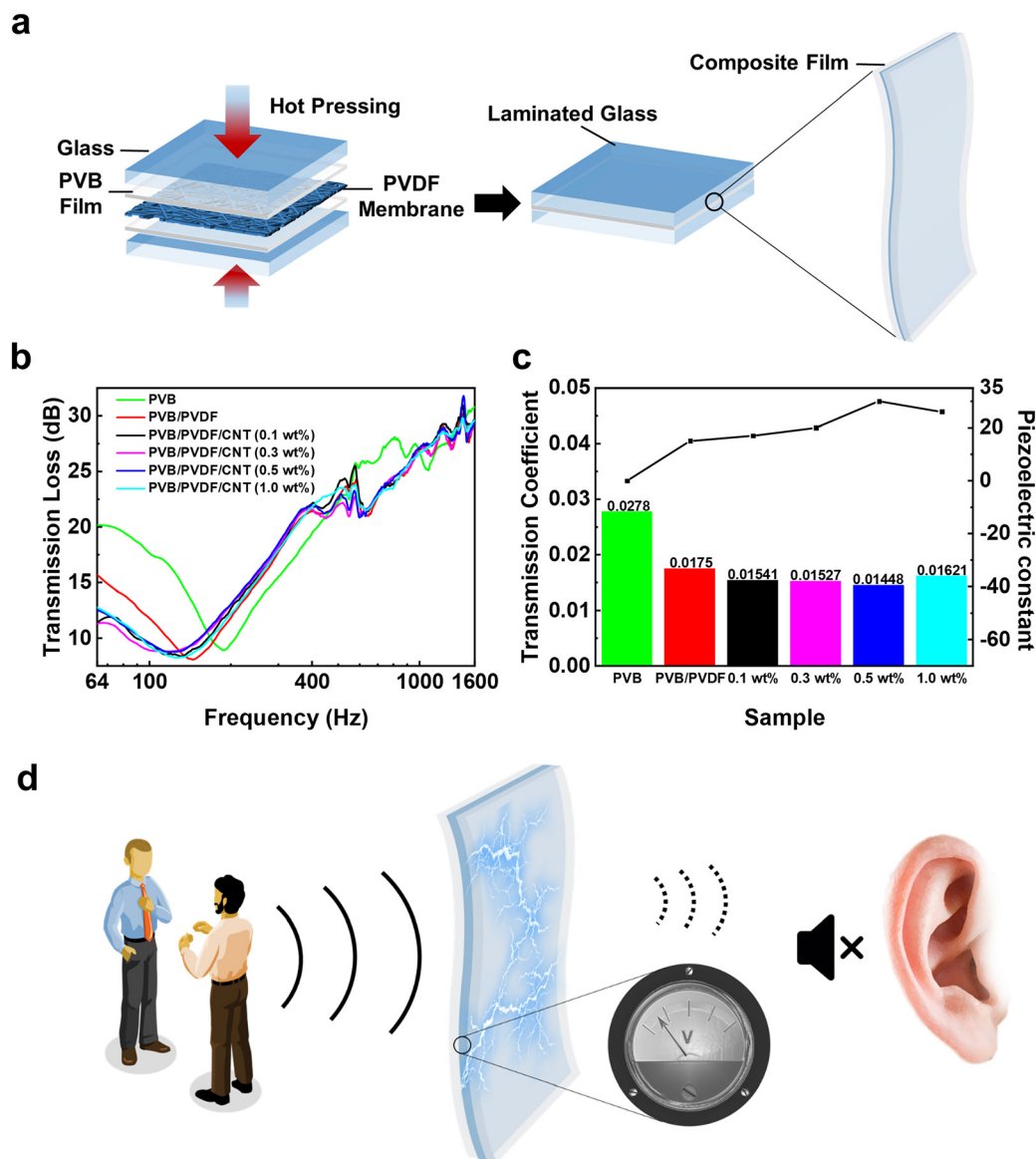


**Fig. 3** (a) The structure and preparation of the PVB/PVDF/PVB composite film and laminated glass. (b) TL of PVB/PVDF composite films with different loading of MWCNTs and (c) average transmission coefficient of all samples in the mass control region and its relationship with its piezoelectricity. (d) Sound insulation mechanism of the composite PVB/PVDF film.

the most valuable reference region, in this region, the sample follows the mass law that the TL of each frequency point increases by 6 dB when the surface mass of the sample is doubled. However, the TL curve that fluctuates after 500 Hz is the first-order modal characteristic of the sample, which does not need to be analysed.

Because the stiffness of the glass is too high, it causes the range of the mass control region to be significantly reduced, and the sound insulation performance of the laminated glass was not measured. It can be seen in the figure that all the composite samples are superior to the single ones in the mass control region (200–500 Hz). Generally, the sound waves pass directly through the fibers because of their porous structure, but when electrospun fibers are incorporated into PVB, the sound waves will collide with the fibers many times (Fig. S4, ESI<sup>†</sup>),

which is attributed to the blocking effect of PVB on the transmission of the sound waves. However, the trend of the TL curve is not consistent with the conclusions of the previous BET test (Table S1, ESI<sup>†</sup>), which is due to the further elimination of sound energy by piezoelectric fibers. It can be seen that the higher is the piezoelectricity of the electrospun PVDF membrane, the higher the TL value of the composite film. The lightweight PVB/PVDF composite glass interlayer film can break the conventional mass law with a transmission loss of over 15 dB in the low frequency region. The increase can reach a maximum of 3.6 dB when the loading of MWCNTs is 0.5 wt%, although its specific surface area and porosity are lower than those of the sample without MWCNTs. TL of PVB composite film containing electrospun non-piezoelectric polyamide 6 (PA6) fiber has been reported in Fig. S8 (ESI<sup>†</sup>). It can be seen that the TL of the PVB/PA6



composite film is superior to that of the pure PVB film, due to the absorption of low-frequency sound energy by the electrospun PA6 fiber with nanoscale diameter, which is much smaller than the diameter of PVDF.<sup>37,38</sup> However, the TL of the PVB/PVDF composite film is significantly higher than that of the PVB/PA6 composite film, indicating that the piezoelectric effect of electrospun nanofiber take the dominant part in the elimination of sound energy. The TL values of all samples at different frequencies in detail are listed in Table S2 (ESI†). The average sound insulation performance of the samples in the mass control region can be measured using the following eqn (2):

$$TL = 10 \log \left( \frac{1}{\tau} \right) = 10 \log \left( \frac{W_1}{W_2} \right) \quad (2)$$

where  $\tau$  is the transmission coefficient of the sample, which is the reciprocal of the ratio of the sound power  $W_1$  incident on the sample and the transmission sound power  $W_2$  through the sample. The percentage reduction of sound power (sound energy) through the sample can be represented by the percentage reduction of  $\tau$ . The average transmission coefficient and their relationship with the piezoelectricity of all samples in the mass control region are shown in Fig. 3c. The average sound energy passing through decreases with the increase of piezoelectricity and it is reduced by 48% when the piezoelectricity of electrospun PVDF membrane reached the maximum. As shown in Fig. 3d, the mechanical vibration energy is first transmitted to the piezoelectric PVDF membrane, and converted into electrical potential energy by the piezoelectric effect. Then, the potential energy is further converted into heat through the network of MWCNTs in an electrospun PVDF membrane to eliminate the sound energy. MWCNTs reinforced the piezoelectricity of the electrospun PVDF membrane and thus improved the sound insulation performance of composite films. However, when their loading exceeds the percolation threshold significantly, a short circuit network can be generated, reducing the energy conversion efficiency.<sup>39</sup> This indicates that the addition of MWCNTs lower than 1.0 wt%

is better to satisfy the requirement of sound insulation. It can also demonstrate that MWCNTs are not simply eliminated sound energy as inorganic particles.

The impact resistance of laminated glass depends on the adhesion of the intermediate layer in the glass. Therefore, the shear test was performed on a universal tensile strength tester (QT-6201S QianTong Instrument Machine Co. Ltd), where the composite PVB film with the dimensions of 12.5 mm (width)  $\times$  25 mm (length) was hot pressed to the corresponding position of the glass and then stretched (Fig. S9a, ESI†). As shown in Fig. S9b (ESI†), the adhesion to glass is not affected by the introduction of the PVDF fiber membrane to the PVB, and the shear strength of all samples exceeds 3 MPa, which fully meets the performance requirements of the interlayer film of the laminated glass. The toughness of the PVDF membrane after hot pressing was also tested. As shown in Fig. S10a and b (ESI†), bended it and then unfolded it, a complete and crease-free PVDF membrane can be observed. In addition, the length of the PVDF has been stretched from 35 mm to 55 mm with an elongation exceeding 55%, indicating that the PVDF membrane after hot pressing is not a brittle material (Fig. S10c and d, ESI†). Then, the sound insulation laminated glass based on the PVB/PVDF composite film was constructed by the hot pressing process. As shown in Fig. 4a, the impact resistances of which were detected by falling ball impact on the samples in 9 cm  $\times$  9 cm size according to AS NZS 2208-1996, a 300 g ball was dropped and the drop height was progressively increased to 45 cm, 60 cm, 75 cm, 90 cm, 120 cm, and 150 cm until the breakage occurred. After testing, all the samples broke at a height of 120 cm, for more accurate experimental results, the ball with the same mass was dropped 5 times from a height of 120 cm and the mass percentage of the broken glass slag was measured (breakage rate). The image of laminated glass after being impacted is shown in Fig. 4b, and the breakage rate is listed in Table S3 (ESI†). As shown in the figure, the breakage rate of all samples is within the range of 2.5% to 2.8%. The impact resistance of the laminated glass is not affected by the

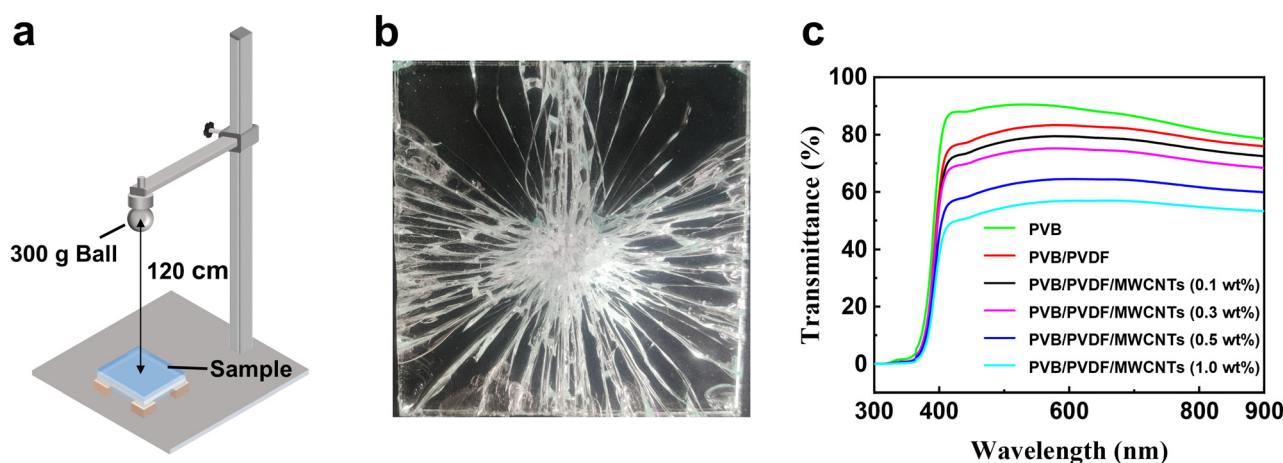


Fig. 4 (a) Falling ball impact test and (b) image of laminated glass after being impacted. (c) The ultraviolet spectrum of all laminated glass with different interlayers.



introduction of a thin electrospun piezoelectric fiber membrane and is sufficient for normal use.

The ultraviolet spectrum of the laminated glass is shown in Fig. 4c. As shown in the figure, when an appropriate amount of MWCNTs are added, the transmittance of composite laminated glass is nearly 80%, which is close to that of the PVB laminated glass. Therefore, this kind of sound insulation laminated safety glass has great application potential, such as in an automobile or architectural glass.

## Conclusions

In summary, a new strategy that uses piezoelectric fibers to improve the sound insulation of materials was proposed. The PVDF/MWCNTs membrane was produced by ES technology, and PVB/PVDF composite film was successfully obtained using the hot pressing process. MWCNTs significantly improved the piezoelectricity of the electrospun PVDF membrane. When the loading of MWCNTs was 0.5 wt%, the piezoelectric coefficient  $d_{33}$  of PVDF/MWCNTs electrospun membrane was 30. The generated electric outputs reached the peak of 2 V. The sound insulation of the glass interlayer film was significantly enhanced in the low-frequency region (200–500 Hz) by introducing piezoelectric PVDF fibers, the TL was over 15 dB and the enhancement reached a maximum of 3.6 dB compared to that of the pure PVB film. The average passing through sound energy was significantly reduced by 48%, which implied the effective blocking out of human low-frequency noise. The PVB/PVDF film-based laminated glass possesses excellent impact resistance and high transmittance, which is sufficient for normal use. The relationship between the piezoelectricity of fibers and sound insulation characteristics is established. These easily available piezoelectric fibers with negligible mass are of great significance to the research and development of sound insulation materials.

## Author contributions

D. H. Chen and S. W. Wang designed the experiments. D. H. Chen and S. Zheng analysed and interpreted the data. D. H. Chen and M. Y. Jing performed the experiments. J. W. Zhang and L. J. Yu drew the schematic diagram. D. H. Chen wrote the draft. S. W. Wang and S. L. Sun provided financial assistance. S. W. Wang and Z. Q. Yu revised the manuscript.

## Conflicts of interest

There are no conflicts to declare.

## Acknowledgements

The authors gratefully acknowledge the funding of this research offered by the National Natural Science Foundation of China (U21A2088, 21204087); Changchun Science and Technology Development Plan Project (21ZY39); Capital construction funds within the budget of Jilin Province in 2023 (2023C044-3); Jilin

Science and Technology Development Project (YDZJ202301-ZYTS542, YDZJ202201ZYTS557, 20220508154RC, 20200403142SF, 20210203111SF).

## References

- 1 H. Slabbekoorn, *Curr. Biol.*, 2019, **29**, R957–R960.
- 2 M. S. Hammer, T. K. Swinburn and R. L. Neitzel, *Environ. Health Perspect.*, 2014, **122**, 115–119.
- 3 M. Yuan, C. Yin, Y. Sun and W. Chen, *Sustainable Cities Soc.*, 2019, **50**, 101678.
- 4 Z. Lei, Y. Wu, J. He, X. Liu, H. Wang, S. Jiang, L. Gu, Q. Zhang, B. Gault, D. Raabe and Z. Lu, *Sci. Adv.*, 2020, **6**, eaba7802.
- 5 F. Pelayo, M. J. Lamela-Rey, M. Muniz-Calvente, M. López-Aenlle, A. Álvarez-Vázquez and A. Fernández-Canteli, *Thin Wall Struct.*, 2017, **119**, 324–331.
- 6 M. Martín, X. Centelles, A. Solé, C. Barreneche, A. I. Fernández and L. F. Cabeza, *Constr. Build. Mater.*, 2020, **230**, 116897.
- 7 M. López-Aenlle, A. Noriega and F. Pelayo, *Composites, Part B*, 2019, **169**, 9–18.
- 8 S. Chen, M. Zang, D. Wang, S. Yoshimura and T. Yamada, *Composites, Part B*, 2017, **122**, 47–60.
- 9 C. Zhang, J. Gong, H. Li and J. Zhang, *Composites, Part B*, 2020, **198**, 108166.
- 10 S. Chen, M. Zang, D. Wang, Z. Zheng and C. Zhao, *Compos. Struct.*, 2016, **138**, 1–11.
- 11 J. Choi, I. Jung and C. Y. Kang, *Nano Energy*, 2019, **56**, 169–183.
- 12 C. Lang, J. Fang, H. Shao, X. Ding and T. Lin, *Nat. Commun.*, 2016, **7**, 11108.
- 13 H. Shi, Y. He, Y. Pan, H. Di, G. Zeng, L. Zhang and C. Zhang, *J. Membr. Sci.*, 2016, **506**, 60–70.
- 14 R. Tu, E. Sprague and H. A. Sodano, *Addit. Manuf.*, 2020, **35**, 101358.
- 15 S. Pan, M. Li, F. Chen, Z. Huang, Q. Shen and L. Zhang, *Adv. Mater. Sci. Eng.*, 2018, **2018**, 1253635.
- 16 Y. Li, M. H. Xu, Y. S. Xia, J. M. Wu, X. K. Sun, S. Wang, G. H. Hu and C. X. Xiong, *Chem. Eng. J.*, 2020, **388**, 124205.
- 17 A. Baji, Y. W. Mai, M. Abtahi, S. C. Wong, Y. Liu and Q. Li, *Compos. Sci. Technol.*, 2013, **88**, 1–8.
- 18 R. K. Singh, S. W. Lye and J. Miao, *Polymer*, 2021, **214**, 123366.
- 19 Y. L. Liu, Y. Li, J. T. Xu and Z. Q. Fan, *ACS Appl. Mater. Interfaces*, 2010, **2**, 1759–1768.
- 20 M. Sharma, G. Madras and S. Bose, *Phys. Chem. Chem. Phys.*, 2014, **16**, 14792–14799.
- 21 S. Yu, Y. Zhang, Z. Yu, J. Zheng, Y. Wang and H. Zhou, *Nano Energy*, 2021, **80**, 105519.
- 22 N. de Jonge, M. Doytcheva, M. Allieux, M. Kaiser, S. A. M. Mentink, K. B. K. Teo, R. G. Lacerda and W. I. Milne, *Adv. Mater.*, 2005, **17**, 451–455.
- 23 D. Mohanta, S. Patnaik, S. Sood and N. Das, *J. Pharm. Anal.*, 2019, **9**, 293–300.
- 24 P. Najmi, N. Keshmiri, M. Ramezanzadeh and B. Ramezanzadeh, *Chem. Eng. J.*, 2021, **412**, 128637.





- 25 S. Sharafkhani and M. Kokabi, *Adv. Compos. Hybrid Mater.*, 2022, **5**, 3081–3093.
- 26 M. Pusty and P. M. Shirage, *J. Alloys Compd.*, 2022, **904**, 164060.
- 27 P. K. Szewczyk, A. Grady, S. K. Kim, L. Persano, M. Marzec, A. Kryshnal, T. Busolo, A. Toncelli, D. Pisignano, A. Bernasik, S. Kar-Narayan, P. Sajkiewicz and U. Stachewicz, *ACS Appl. Mater. Interfaces*, 2020, **12**, 13575–13583.
- 28 C. M. Wu and M. H. Chou, *Compos. Sci. Technol.*, 2016, **127**, 127–133.
- 29 A. Huang, F. Liu, Z. Cui, H. Wang, X. Song, L. Geng, H. Wang and X. Peng, *Compos. Sci. Technol.*, 2021, **214**, 108980.
- 30 A. Moheman, M. S. Alam and A. Mohammad, *Adv. Colloid Interface Sci.*, 2016, **229**, 1–24.
- 31 D. R. Barbero and N. Boulanger, *ACS Nano*, 2017, **11**, 9906–9913.
- 32 J. Xie, H. Liu, J. Hu, X. Zhao, S. Song, S. Sun and M. Zhang, *Mater. Adv.*, 2022, **3**, 6619–6627.
- 33 M. Sharma, V. Srinivas, G. Madras and S. Bose, *RSC Adv.*, 2016, **6**, 6251–6258.
- 34 F. Orudzhev, S. Ramazanov, D. Sobola, P. Kaspar, T. Trčka, K. Částková, J. Kastyl, I. Zvereva, C. Wang, D. Selimov, R. Gulakhmedov, M. Abdurakhmanov, A. Shuaibov and M. Kadiev, *Nano Energy*, 2021, **90**, 106586.
- 35 C. Y. Lai, A. Groth, S. Gray and M. Duke, *Water Res.*, 2014, **57**, 56–66.
- 36 H. Song, W. Song, J. H. Song, V. M. Torrejon, Q. Xia and B. P. Singh, *J. Nanomater.*, 2022, **2022**, 1–17.
- 37 T. Ulrich and J. P. Arenas, *Sustainability*, 2020, **12**, 2361.
- 38 M. Park, H. K. Park, H. K. Shin, D. Kang, B. Pant, H. Kim, J. K. Song and H. Y. Kim, *J. Nanosci. Nanotechnol.*, 2019, **19**, 3558–3563.
- 39 S. Pan, M. Li, F. Chen, Z. Huang, Q. Shen and L. Zhang, *Adv. Mater. Sci. Eng.*, 2018, **2018**, 1–7.

